Non-Abelian Gauge Fields in Photonic Cavities and Photonic Superfluids

H. Terças,[1] H. Flayac,[2] D. D. Solnyshkov,[1] and G. Malpuech[1]
[1]*Institut Pascal, PHOTON-N2, Clermont Université, Blaise Pascal University, CNRS, 24 Avenue des Landais, 63177 Aubière Cedex, France*
[2]*Institute of Theoretical Physics, École Polytechnique Fédérale de Lausanne EPFL, CH-1015 Lausanne, Switzerland*
(Received 11 March 2013; revised manuscript received 19 November 2013; published 11 February 2014)

We show that the TE-TM modes splitting and the structure anisotropy of a semiconductor microcavity combine into a non-Abelian gauge field for exciton-polaritons or cavity photons. The field texture can be tuned simply by rotating the sample and ranges continuously from a Rashba to a monopolar field. In the noninteracting regime, the latter leads to remarkable focusing and conical diffraction effects. In the interacting regime, the spin-orbit coupling induces a breakdown of superfluidity. The spatially homogeneous flows become unstable and dynamically evolve into spin textured states, such as stripes or domain walls.

DOI: 10.1103/PhysRevLett.112.066402 PACS numbers: 71.36.+c, 67.85.Fg, 71.70.Ej

The creation of synthetic gauge fields has been seriously addressed recently [1–4]. In condensed matter systems, gauge fields due to spin-orbit coupling (SOC) play a central role in the spin-Hall effect [5,6], topological insulators [7,8] and semiconductor-based spintronics [9]. Artificial magnetic fields in atomic Bose-Einstein condensates (BECs) allow the formation of vortices without stirring [1], while an artificial field of the Rashba type leads to the formation of spin domains [2]. In purely photonic systems [10] synthetic gauge fields have been proposed [11,12] and produced [13], forming a basis for topologically protected states of a spin-Hall system. The photonic de Haas–van Alphen effect was shown [14] in the presence of synthetic magnetic fields [15]. Photonic topological insulators have been experimentally demonstrated [16,17].

In confined photonic structures, both photons and mixed particles such as exciton-polaritons experience spin-orbit coupling. It originates from the splitting between TE and TM modes [18,19] and is characterized by a k^2 scaling and a double azimuthal dependence. While the TE-TM field leads to several fascinating effects, such as the optical spin-Hall effect [20–22] or the acceleration of magnetic monopole analogs [23,24], it cannot be integrated in the system Hamiltonian as a minimal coupling. In other words, it does not satisfy gauge transformations. The dispersion of the elementary excitations of a polariton BEC in the presence of the TE-TM splitting is anisotropic [25], but the dynamics of the condensate is stable. The physical reason is that the TE-TM field does not break the spatial inversion symmetry, contrary to Rashba or Dresselhaus SOC [26–28]. In atomic condensates with a SOC linear in k, the ground state can be plane waves or stripes [29] with or without trapping, while vortices can also appear in the trapped case [30,31]. By contrast, the TE-TM field in polariton BECs allows a homogeneously spin-polarized ground state.

In this Letter, we show how to create an effective gauge field for propagating photons or polariton condensates by combining the TE-TM splitting and an additional splitting between linear polarizations associated with crystallographic axes (constant effective magnetic field [32]). A flowing condensate can be created with a wave vector $\mathbf{k}_0$ by adjusting the angle between the laser beam and the cavity (normal) (see Fig. 1). Around a critical velocity $\mathbf{v}_* = \hbar\mathbf{k}_*/m$, for which the static in-plane field Ω associated with crystallographic axes [18] and TE-TM fields exactly compensate, the effective field acting on the pseudospin is a non-Abelian gauge field of the Rashba kind. The orientation of the field $\Omega = \Omega(\cos\varphi, \sin\varphi)$ in the (k_x, k_y) plane can be tuned by simply rotating the sample as illustrated in Fig. 1. In the noninteracting photonic regime, this field leads to both focusing and conical diffraction effects [33–36]. In the interacting regime, it makes the homogeneous superfluid flow unstable, in close analogy with atomic condensates with synthetic gauge fields. By investigating the properties of the collective excitations of a condensate polarized along the static field, we show that the gauge field makes the homogeneous superfluid flow unstable (i) against transverse excitations in a limited region below k_* and (ii) against both transverse and

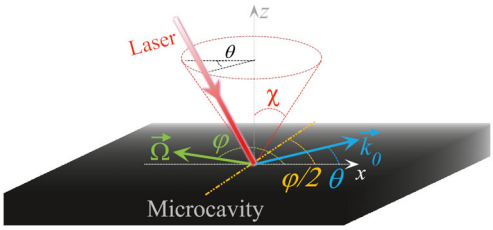

FIG. 1 (color online). Scheme of the experimental configuration necessary to produce a controllable gauge field. The angle between the crystallographic axis (the effective magnetic field Ω) and the horizontal is $\varphi/2$ (φ). A laser with a vertical inclination χ making an angle θ with the horizontal produces a propagating polariton beam with wave vector $\mathbf{k}_0 = (\omega_0/c)\sin\chi(\cos\theta, \sin\theta)$, where ω_0 is the laser frequency and c is the light speed.

longitudinal excitations for wave vectors above k_*, depending on the condensate polarization. These two instability mechanisms trigger the formation of spin stripes and domain walls. Remarkable features occur when the polarization of the condensate is perpendicular to the static field. In such a case, a slowly propagating flow is unstable, whereas the superfluid motion is recovered above a critical velocity: an unexpected breakdown of superfluidity occurs in the subsonic regime.

We consider the motion of a bosonic fluid described by the spinor Gross-Pitaevskii equation

$$i\hbar\frac{\partial\mathbf{\Psi}}{\partial t}=\hat{H}_0\mathbf{\Psi}+\alpha_1\mathbf{\Psi}^\dagger\mathbf{\Psi}\mathbf{\Psi}+\alpha_2\mathbf{\Psi}\sigma_x\mathbf{\Psi}^\dagger\mathbf{\Psi}, \quad (1)$$

where $\mathbf{\Psi}=(\psi_+,\psi_-)^T$, α_1 and α_2 are the intra- and interspin interaction constants, and σ_x is the antidiagonal Pauli matrix. The single particle Hamiltonian, valid for both weakly coupled photons and polaritons in the parabolic approximation, is written as

$$\hat{H}_0=\begin{bmatrix}-\frac{\hbar^2\nabla^2}{2m} & -\frac{\Omega}{2}e^{-i\varphi}+\beta(\partial_y-i\partial_x)^2\\ -\frac{\Omega}{2}e^{i\varphi}+\beta(\partial_y+i\partial_x)^2 & -\frac{\hbar^2\nabla^2}{2m}\end{bmatrix}, \quad (2)$$

where $\beta=\hbar^2/(2m_r)$ is the strength of the TE-TM field, m_ℓ and m_t represent the longitudinal and transverse polariton masses, $m_r=m_\ell m_t/(m_t-m_\ell)$ and $m=m_\ell m_t/(m_\ell+m_t)$ is the reduced polariton mass. The Hamiltonian (2) describes an ideal polariton BEC, in the limit of a very long lifetime, decoupled from the thermal bath. Diagonalization leads to the following single-particle spectrum

$$\epsilon_\pm=\frac{\hbar^2k^2}{2m}\pm\sqrt{\beta^2k^4-\beta\Omega k^2\cos(2\theta_k-\varphi)+\frac{\Omega^2}{4}}, \quad (3)$$

where $k=\sqrt{k_x^2+k_y^2}$ and $\mathbf{k}=k(\cos\theta_k,\sin\theta_k)$. Its features are summarized in Fig. 2 for $\varphi=0$. Fig. 2(a) depicts $\epsilon_\pm$ along k_x ($\theta_k=0$), exhibiting the crossing of the two branches at $k_*=\sqrt{\Omega/2\beta}$, the point at which the TE-TM field and Ω exactly compensate. For $k_x<k_{c1}=\sqrt{\Omega m_\ell/2\beta m_t}$, the energy is a monotonic function of k_y [Fig. 2(b)]; on the other hand, for $k_x>k_{c1}$ the lower branch $\epsilon_-(k_y)$ bends and the parametric process $k_y:\ 0\to\pm\kappa_p$, with

$$\kappa_p=\left\{\frac{k_0^2/(1+m/2m_r)-k_*^2(1-m/2m_r)}{1-m/4m_r}\right\}^{1/2}, \quad (4)$$

conserving both energy and momentum is possible [see Figs. 2(c), and 2(d)], leading to a transverse instability of a superfluid flow. The dispersion is locally linear [Fig. 2(d)]

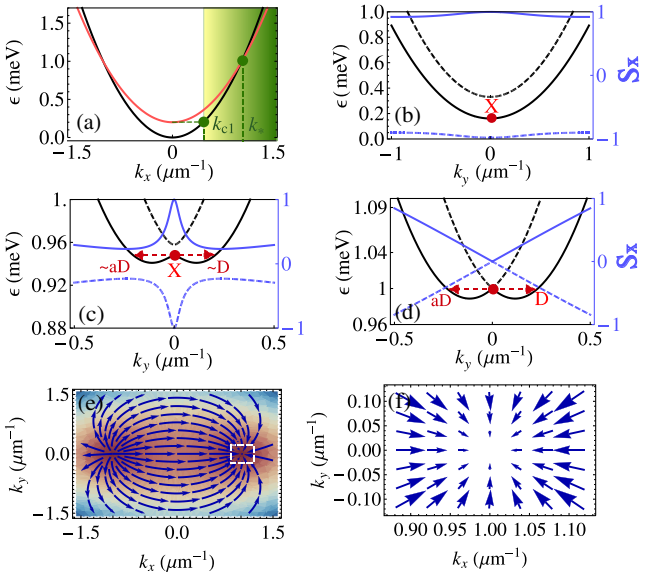

FIG. 2 (color online). Polariton dispersion relation for $\varphi=0$ ($-\Omega/2$ taken as zero reference). (a) Dispersion along the x direction showing the two polariton branches $\epsilon_\pm$ crossing at the magic point $k_*=\sqrt{\Omega/2\beta}$. The green-shadowed rectangle defines the region $|\mathbf{k}_0-\mathbf{k}_*|\le k_{c1}$, where the transverse dispersion bends. Panels (b),(c), and (d) show the dispersion along the y direction (black) and the corresponding x projection of the pseudospin (blue and gray) for $k_x=\{0.4,0.97,1.0\}$ μm. In (c), a parametric process $k_y:\ 0\to\pm\kappa_p$ occurs between an X-polarized mode and a diagonal (D) and an antidiagonal (aD) mode. In (d), we observe the linear intersection of two branches crossing each other at $k_y=0$. Panel (e) depicts the field texture of Eq. (2) in the reciprocal space and panel (f) zooms around the wave vector k_*. Parameters used are $m=4.5\times10^{-5}m_e$, $\Omega=0.2$ meV, and $\beta=0.1$ meV μm^2, yielding $k_*=1.0$ μm^{-1}.

near $q=0$, $\epsilon_\pm-\epsilon(k_*)\simeq\hbar^2q^2/(2m)\pm\sqrt{\beta\Omega}q$, with $\mathbf{q}=\mathbf{k}-\mathbf{k}_*$, where $\mathbf{k}_*=\pm\sqrt{\Omega/2\beta}(\cos\varphi/2,\sin\varphi/2)$ is the compensation wave vector. This dispersion is typical for a spin-orbit coupling of the Rashba type. For particles propagating at a wave vector $\mathbf{k}_0$, the Hamiltonian can be written as

$$\hat{H}_0=\frac{\hbar^2}{2m}(\mathbf{q}^2+\kappa_x\boldsymbol{\sigma}\cdot\mathbf{q}+\kappa_y(\boldsymbol{\sigma}\times\mathbf{q})\cdot e_\mathbf{z})-\frac{\delta}{2}\sigma_x, \quad (5)$$

where $\kappa_x=2m\sqrt{\beta\Omega}/\hbar^2\cos\varphi/2$, $\kappa_y=2m\sqrt{\beta\Omega}/\hbar^2\sin\varphi/2$ and $\delta=2\beta(k_*^2-k_0^2)$. In the region $|\mathbf{k}_0-\mathbf{k}_*|\le k_*-k_{c1}$ [shadowed in Fig. 2(a)], the terms scaling linearly in q dominate. Contrary to the TE-TM SOC in Eq. (2), Hamiltonian (5) is a true gauge-field, minimally coupled Hamiltonian, where κ_x and κ_y represent the magnitude of the monopolar- and Rashba-field coupling constants. The gauge field texture $\mathbf{S}(\mathbf{k})$ for the particular case of a horizontal magnetic field ($\varphi=0$) is illustrated in Fig. 2(e) [zoomed in Fig. 2(f)]. A simple rotation of the sample results in more

general field textures, related by the transformation $\mathbf{S}'(\mathbf{k}) = \mathcal{R}(\varphi)\mathbf{S}[\mathcal{R}(-\varphi/2)\mathbf{k}]$, where $\mathcal{R}(\varphi)$ is the 2×2 rotation matrix (see also [37]). Hereinafter, we consider the case $\varphi = 0$. To illustrate the effect of gauge field in Eq. (5), we consider photons (polaritons) propagating at the magic wave vector $\mathbf{k}_0 = k_*\mathbf{e_x}$ or close to it, i.e., $\delta = 0$ (Fig. 3). (i) A Gaussian defect potential $U(r) = U_0 \exp(-r^2/a^2)$ with $a = 10$ μm, scatters elastically the flow. Most of the light shows a weak wave vector change of the order of $2\pi/a$. Downstream from the defect, the particles with diagonal polarization are pulled to the left, and those with antidiagonal polarization are pushed to the right given their opposite group velocity projection v_y [see Fig. 2(d) for dispersion and the Supplemental Material [37] for more details]. In fact, the defect focuses the beam, as if light was "bent" by it [see Figs. 3(a) and 3(b)]. This is quite remarkable, since focusing is obtained despite the defect being impenetrable. (ii) Conical diffraction is obtained by exciting the region around k_* with a circularly polarized pulsed Gaussian pump [Figs. 3(c) and 3(d)]. The physical origin of Hamilton's conical diffraction [33] is a singularity in k space (diabolical point). In the original experiments, it occurred due to polarization splitting (birefringence) [34,35]. But the Dirac points in graphene [36] or the crossing point of a Rashba Hamiltonian [as in Fig. 2(d)] are also examples of diabolical points. (iii) The fourfold spin pattern, associated with the spin-Hall effect (from a linearly polarized Gaussian pump centered at $k = 0$) due to the TE-TM field [20,22], is replaced by a twofold pattern [see Figs. 3(e) and 3(f)] induced by the different symmetry of Eq. (5), when the pump is centered at k_*.

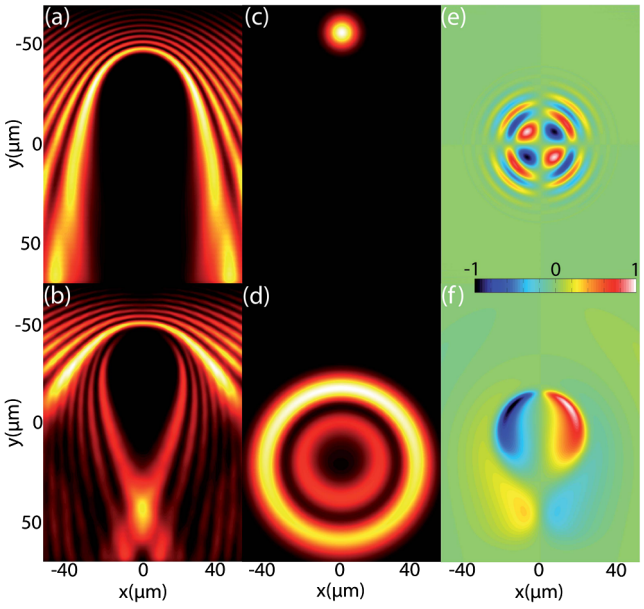

FIG. 3 (color online). Effects of the gauge field: (a),(b) Lensing effect with a linearly polarized polariton flow ($\mathbf{k}_0 = \mathbf{k}_*$) encountering a potential barrier of size $a = 10$ μm (a) in the absence and (b) in the presence of the effective magnetic fields. The color map shows the total density $n = n_+ + n_-$. (c),(d) Conical diffraction under circularly polarized pulsed excitation at $\mathbf{k}_0 = \mathbf{k}_*$: (c) $t = 0$ ps and (d) $t = 50$ ps. (e),(f) Polarization domains. Gaussian linearly polarized pulsed excitation (e) at $\mathbf{k}_0 = \mathbf{0}$ for $\Omega = 0$ and (f) $\mathbf{k} = \mathbf{k}_*$ for $\Omega \neq 0$. The color map shows the circular polarization degree $\rho_c = (n_+ - n_-)/(n_+ + n_-)$.

Next, we investigate the effect of interparticle interactions. First, in contrast to the atomic BECs with linear in k SOC [29], a homogeneous, linearly polarized polariton condensate at rest remains stable in the presence of the SOC introduced in Eq. (2) for $\Omega > 0$, provided that $m_\ell < m_t$ and $|\alpha_1| > |\alpha_2|$, which is the case in experiments. The particular case $\Omega = 0$ has been investigated in [25]. The situation is dramatically modified if the homogeneous condensate is put in motion in the vicinity of k_*. The collective excitations of a polariton BEC propagating with velocity $\mathbf{v}_0 = \hbar\mathbf{k}_0/m$ can be determined by linearizing (1) with $\mathbf{\Psi} = e^{i(\mathbf{k}_0\cdot\mathbf{r}-\mu t/\hbar)}[\mathbf{\Psi}_0 + \sum_{\mathbf{q}}(\mathbf{u}_\mathbf{q}e^{i(\mathbf{q}\cdot\mathbf{r}-\omega t)} + \mathbf{v}^*_\mathbf{q}e^{-i(\mathbf{q}\cdot\mathbf{r}-\omega t)})]$. For a linearly polarized condensate, $\mathbf{\Psi}_0 = (n_+, n_-)^T = n_0(e^{-i\eta}, e^{+i\eta})^T$ with polarization angle η [37]. A condensate is X (Y) polarized for $\eta = 0$ ($\eta = \pi/2$), and the associated pseudospin is $\mathbf{S}_0 = n_0\mathbf{e_x}$ ($\mathbf{S}_0 = -n_0 e_\mathbf{x}$) [38]. The chemical potential includes the interaction and the "magnetic" energy of the condensate

$$\mu = (\alpha_1 + \alpha_2)n_0 - \frac{1}{2}(\Omega - 2\beta k_0^2\cos 2\theta)\cos 2\eta. \quad (6)$$

We consider a BEC propagating with wave vector $\mathbf{k}_0 = k_0\mathbf{e_x}$ and velocity $v_0 = \hbar k_0/m$ below the critical Landau velocity. Let us discuss the case of a X-polarized BEC first. The spectrum of the elementary excitations contains four anisotropic branches, two with positive and two with negative energies: $\pm\epsilon^{L,U}(\mathbf{q})$, where the positive Doppler-shifted lower (L) and upper (U) branches can be written in the long wavelength limit $q \sim 0$ as

$$\epsilon_x^L \simeq \hbar c_\ell^L|q_x| + \frac{\hbar^2 k_0}{m_\ell}q_x, \qquad \epsilon_y^L \simeq \hbar c_\ell^L\sqrt{\frac{k_{c1}^2 - k_0^2}{k_*^2 - k_0^2}}|q_y|$$
$$\epsilon_x^U \simeq \Delta_1 + \frac{\hbar^2 q_x^2}{2m_t}\zeta + \frac{\hbar^2 k_0}{m_t}q_x, \quad \epsilon_y^U \simeq \left\{\Delta_1^2 + \frac{\hbar^2 q_y^2}{m_t}\Delta_2\right\}^{1/2}, \quad (7)$$

where x, y mark corresponding projections, $c_{\ell,t}^L = [(\alpha_1 + \alpha_2)n/m_{\ell,t}]^{1/2}$ are the two sound speeds, $\Delta_1 = \sqrt{\delta[\delta + 2(\alpha_1 - \alpha_2)n]}$, $\zeta = [\delta + (\alpha_1 - \alpha_2)n]/\Delta_1$, and Δ_2 can be found in Ref. [37]. Equation (7) allows us to understand the onset of both transverse (T) and longitudinal (L) instabilities, as illustrated in Fig. 4. For $k < k_{c1}$, all the branches are real and no instability takes place. The X-polarized condensate is therefore stable and superfluid. For $k_{c1} < k_0 < k_*$, ϵ_y^L becomes complex, corresponding to the onset of a T instability [ϵ_x^L and ϵ_y^L in Figs. 4(a), and 4(b)]. The most unstable mode appears at κ_p [parametric process

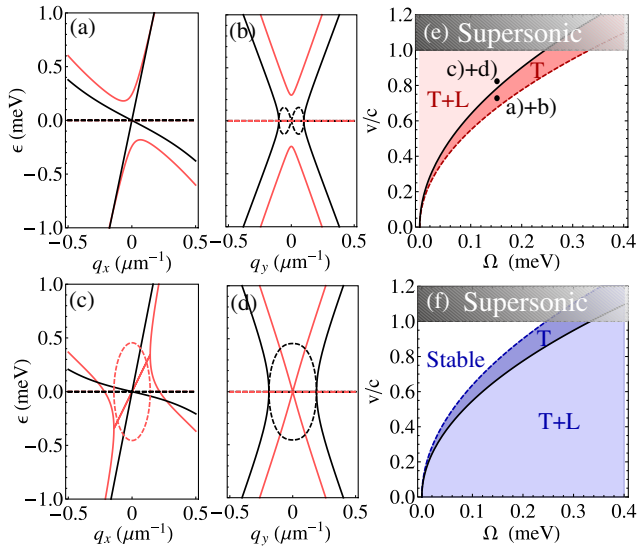

FIG. 4 (color online). From (a) to (d): Transverse (T) and longitudinal (L) instabilities for a X-polarized condensate in the subsonic regime: real (solid) and imaginary (dashed) parts. Black (red and gray) lines depicting the lower (upper) branches $\epsilon^L_{x,y}$ ($\epsilon^U_{x,y}$). T instability: ϵ_x [panel (a)] and ϵ_y [panel (b)] for $k_0 = 0.93k_* > k_{c1}$. $T + L$ instability: ϵ_x [panel (c)] and ϵ_y [panel (d)] for $k_0 = 1.12k_*$. Stability diagram for X- [panel (e)] and Y-polarized [panel (f)] condensates: $v_* = \hbar k_*/m$ (black line), $v_{c1} = \hbar k_{c1}/m$ (red and light gray) and $v_{c2} = \hbar k_{c2}/m$ (blue and light gray). The points correspond to the parameters used in panels (a) and (b) and (c) and (d). We have considered $\alpha_1 n = 2.5$ meV and $\alpha_2 = -0.2\alpha_1$, $\Omega = 0.15$ meV and $\beta = 0.075$ meV μm^2.

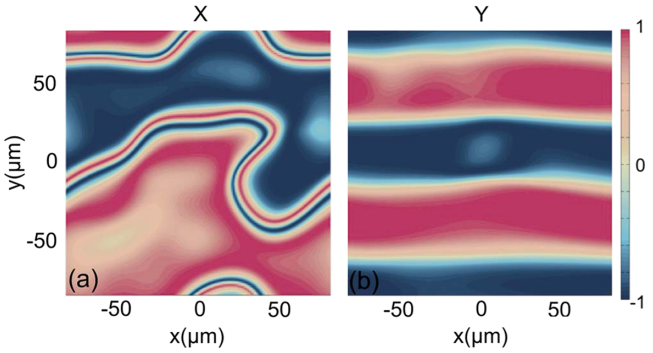

FIG. 5 (color online). Snapshots of the diagonal polarization degree $\rho_D = (n_D - n_{aD})/(n_D + n_{aD})$ after the onset of instabilities. (a) X-polarized BEC at $v_0/c = 0.6$ and (b) Y-polarized BEC at $v_0/c = 0.45$. We have used $\Omega = 0.1$ meV and $\beta = 0.1$ meV μm^2.

conserves both energy and momentum; see Figs. 2(c), and 2(d)], but shifts to $q_y = \pm\kappa_p/2$ for $\mu > \Omega$. For $k_0 > k_*$, $\delta < 0$, and Δ_1 is imaginary, which implies an L instability in the upper branch ϵ^U_x [Fig. 4(c)], but the T instability remains as well [Fig. 4(d), $T + L$ instability]. Above $k_0 > k_{2c} = k_*\sqrt{m_t/m_\ell}$, the most unstable mode is observed for $\mathbf{q} = \mathbf{0}$, similar to the zero wave-vector instability discussed for atomic BECs (see, e.g., Ref. [29]). The substantial difference is that this instability is only achieved for a propagating (and not for a static) condensate. These results are summarized in Fig. 4(e). Increasing the velocity, the system evolves from superfluid to transversally (T), transversally and longitudinally ($T + L$) unstable to finally reach the supersonic regime $v_0 > c = c_\ell c_t/(c_\ell + c_t)$.

The even more intriguing case of a Y-polarized BEC is summarized in Fig. 4(f). For low wave vectors, namely, $k_0 < k_{c1}$, the spin is antialigned with the static field and the system is $T + L$ unstable. Above k_*, the imaginary part of the energy vanishes in the x direction, and only the T instability remains. At wave vectors higher than the second critical wave vector k_{2c}, the system becomes stable. This counterintuitive result simply means that superfluidity breaks down when the flow velocity is decreased or when particle density is increased.

To confirm the previous results, we performed numerical simulations using Eq. (1). For X-polarized condensates, we observe the formation of stripes along the transverse direction for $k_0 > k_{c1}$, illustrating the onset of a T instability (not shown, see Ref. [37]) and the formation of spin domain walls for $k_0 > k_*$ through the $T + L$ instability mechanism [Fig. 5(a)]. For Y polarized BEC, the T instability is observed for $k_* > k_0 > k_{c2}$ [Fig. 5(b)], while the $T + L$ is obtained for $k_0 < k_*$ [37]. At late stages, the instability saturates and the domain wall breaks into pairs of half vortices, the elementary topological defects in spin-anisotropic BECs [39] (see [37] for movie). The T instability (stripes) develops slower, which can be understood from the polarization of the excitations. A process of the type q_y: $0 \to \pm\kappa_p/2$ occurs between an X and two almost diagonal ($\sim D$ and $\sim aD$) states (Fig. 2), for which the difference of polarizations is $\Delta\eta \simeq \pi/4$ giving a factor $\cos^2(2\Delta\eta) \ll 1$ [10,40]. The longitudinal instability develops faster, since the process q_x: $0 \to \pm\kappa_x$ conserves polarization [$\cos^2(2\Delta\eta) = 1$]. Our results reveal a curious difference with respect to atomic BECs, where exotic phases are formed in static systems [29–31].

To conclude, we have shown that a non-Abelian effective gauge field appears for a propagating polariton condensate as an interplay of the TE-TM splitting and a constant in-plane field. The configuration we propose can be easily obtained in microcavities where both static and TE-TM fields are present. This gauge field leads to lensing effects, conical diffraction, polarization patterns, and to the instability of superfluid flow accompanied by the formation of spin-textured states.

We thank I. A. Shelykh for discussions. This work was supported by the projects "ANR QUANDYDE," IRSES POLAPHEN, and Labex GANEX.

[1] Y.-J. Lin, R. L. Compton, K. Jiménez-García, J. V. Porto, and I. B. Spielman, Nature (London) **462**, 628 (2009).
[2] Y.-J. Lin, K. Jiménez-García, and I. B. Spielman, Nature (London) **471**, 83 (2011).
[3] M. Aidelsburger, M. Atala, S. Nascimbène, S. Trotzky, Y.-A. Chen, and I. Bloch, Phys. Rev. Lett. **107**, 255301 (2011).
[4] S. Chen, J.-Y. Zhang, S.-C. Ji, Z. Chen, L. Zhang, Z.-D. Du, Y. Deng, H. Zhai, and J.-W. Pan, Phys. Rev. Lett. **109**, 115301 (2012).
[5] Y. K. Kato, R. C. Meyers, A. C. Gossard, and D. D. Awschalom, Science **306**, 1910 (2004).
[6] M. Konig, S. Wiedmann, C. Brune, A. Roth, H. Buhmann, L. W. Molenkamp, X.-L. Qi, and S.-C. Zhang, Science **318**, 766 (2007).
[7] C. L. Kane and E. J. Mele, Phys. Rev. Lett. **95**, 146802 (2005).
[8] B. A. Bernevig, T. L. Hughes, and S.-C. Zhang, Science **314**, 1757 (2006).
[9] J. D. Koralek *et al.*, Nature (London) **458**, 610 (2009).
[10] I. Carusotto and C. Ciuti, Rev. Mod. Phys. **85**, 299 (2013).
[11] R. O. Umucalilar and I. Carusotto, Phys. Rev. A **84**, 043804 (2011).
[12] M. Hafezi, E. A. Demler, M. P. Lukin, and J. M. Taylor, Nat. Phys. **7**, 907 (2011).
[13] M. Hafezi, J. Fan, A. Migdall, and J. Taylor, Nat. Photonics **7**, 1001 (2013).
[14] K. Fang, Z. Yu, and S. Fan, Opt. Express **21**, 18 216 (2013).
[15] M. C. Rechtsman, J. M. Zeuner, A. Tnnermann, S. Nolte, M. Segev, and A. Szameit, Nat. Photonics **7**, 153 (2012).
[16] M. C. Rechtsman, J. M. Zeuner, Y. Plotnik, Y. Lumer, D. Podolsky, F. Dreisow, S. Nolte, M. Segev, and A. Szameit, Nature (London) **496**, 196 (2013).
[17] N. Jia, A. Sommer, D. Schuster, and J. Simon, arXiv:1309.0878.
[18] I. A. Shelykh, A. V. Kavokin, Y. G. Rubo, T. C. H. Liew, and G. Malpuech, Semicond. Sci. Technol. **25**, 013001, (2010).
[19] A. Kuther, M. Bayer, T. Gutbrod, A. Forchel, P. A. Knipp, T. L. Reinecke, and R. Werner, Phys. Rev. B **58**, 15744 (1998).
[20] H. Flayac, D. D. Solnyshkov, I. A. Shelykh, and G. Malpuech, Phys. Rev. Lett. **110**, 016404 (2013).
[21] A. Kavokin, G. Malpuech, and M. Glazov, Phys. Rev. Lett. **95**, 136601 (2005).
[22] C. Leyder, M. Romanelli, J. Ph. Karr, E. Giacobino, T. C. H. Liew, M. M. Glazov, A. V. Kavokin, G. Malpuech, and A. Bramati, Nat. Phys. **3**, 628 (2007).
[23] D. D. Solnyshkov, H. Flayac, and G. Malpuech, Phys. Rev. B **85**, 073105 (2012).
[24] R. Hivet, H. Flayac, D. D. Solnyshkov, D. Tanese, T. Boulier, D. Andreoli, E. Giacobino, J. Bloch, A. Bramati, G. Malpuech, and A. Amo, Nat. Phys. **8**, 724 (2012).
[25] I. A. Shelykh, Y. G. Rubo, G. Malpuech, D. D. Solnyshkov, and A. Kavokin, Phys. Rev. Lett. **97**, 066402 (2006).
[26] J. Dalibard, F. Gerbier, G. Juzeliünas, and P. Öhberg, Rev. Mod. Phys. **83**, 1523 (2011).
[27] Y. A. Bychkov and E. I. Rashba, J. Phys. C **17**, 6039 (1984).
[28] G. Dresselhaus, Phys. Rev. **100**, 580 (1955).
[29] C. Wang, C. Gao, C.-M. Jian, and H. Zhai, Phys. Rev. Lett. **105**, 160403 (2010).
[30] S. Sinha, R. Nath, and L. Santos, Phys. Rev. Lett. **107**, 270401 (2011).
[31] H. Hu, B. Ramachandhran, H. Pu, and X. J. Liu, Phys. Rev. Lett. **108**, 010402 (2012).
[32] L. Klopotowski, M. D. Martin, A. Amo, L. Vina, I. A. Shelykh, M. M. Glazov, G. Malpuech, A. V. Kavokin, and R. Andre, Solid State Commun. **139**, 511 (2006).
[33] W. R. Hamilton, Trans. R. Irish Acad. **17**, 1 (1837).
[34] H. Lloyd, Trans. R. Irish Acad. **17**, 145 (1837).
[35] M. V. Berry, M. R. Jeffrey, and J. G. Lunney, Proc. R. Soc. A **462**, 1629 (2006).
[36] Or Peleg, G. Bartal, B. Freedman, O. Manela, M. Segev, and D. Christodoulides, Phys. Rev. Lett. **98**, 103901 (2007).
[37] See Supplemental Material at http://link.aps.org/supplemental/10.1103/PhysRevLett.112.066402 for a schematic explanation of the lensing effect and further details on the linearization of Eq. (1).
[38] H. Flayac, D. D. Solnyshkov, and G. Malpuech, Phys. Rev. B **83**, 193305 (2011).
[39] Yu. G. Rubo, Phys. Rev. Lett. **99**, 106401 (2007).
[40] A. Kavokin and G. Malpuech, *Cavity Polaritons*, edited by V. M. Agranovich (Elsevier, New York, 2003), Chap. 5.